Short-range and long-range magnetic order in $Fe(Te_{1.5}Se_{0.5})O_5Cl$

E. S. Kozlyakova,[1,2] K. N. Denisova,[1,3] A. A. Eliseev,[1] A. V. Moskin,[1] A. Y. Akhrorov,[1] P. S. Berdonosov,[1]
V. A. Dolgikh,[1] B. Rahaman,[4] S. Das,[5] T. Saha-Dasgupta,[5] P. Lemmens,[3] A. N. Vasiliev,[1,6,7] and O. S. Volkova[1,7]
[1]*Lomonosov Moscow State University, Moscow, Russia*
[2]*National University of Science and Technology "MISiS," Moscow 119049, Russia*
[3]*Technische Universität Braunschweig, Braunschweig, Germany*
[4]*Department of Physics, Aliah University, New Town, Kolkata, India*
[5]*S.N. Bose National Centre for Basic Sciences, Salt Lake, Kolkata, India*
[6]*National Research South Ural State University, Chelyabinsk 454080, Russia*
[7]*Ural Federal University, 620002 Ekaterinburg, Russia*

(Received 24 June 2020; revised 16 November 2020; accepted 20 November 2020; published 3 December 2020)

Considerable attention has been paid recently to $FeTe_2O_5Cl$ due to reduced dimensionality and frustration in the magnetic subsystem, succession of phase transitions, and multiferroicity. The efforts to grow its selenite sibling resulted in the mixed halide compound $Fe(Te_{1.5}Se_{0.5})O_5Cl$, which was found crystallizing in a different structural type and possessing properties drastically different from those of a parent system. Its magnetic subsystem features weakly coupled $Fe^{3+}-Fe^{3+}$ dimers showing the regime of short-range correlations at $T_M \sim 70$ K and long-range order at $T_N = 22$ K. In a magnetically ordered state, sizable spin-orbital interactions lead to a small canting of Fe^{3+} moments. Magnetic dipole-dipole interactions contribute significantly to the experimentally observed orientation of magnetization easy axis in the *ac* plane. The first principles calculations of leading exchange interactions were found in agreement with measurements of thermodynamic properties and Raman spectroscopy.

DOI: 10.1103/PhysRevB.102.214405

I. INTRODUCTION

The iron tellurate halides, $FeTe_2O_5X$ (X = Cl, Br), are the prototype examples of compounds where the combination of lone-pair elements with transition metals results in magnetoelectric effects [1–5]. The structural key units of these species are Fe_4O_{16} clusters organized by $Fe^{3+}O_6$ octahedra connected via *cis* and *trans* edges. The clusters are linked by $Te_4O_{10}X_2$ groups forming layers interacting only through weak van der Waals forces [1]. The interlayer interactions drive these materials into a long-range magnetically ordered state which takes place through a succession of two incommensurate antiferromagnetic structures. In both compounds, the low temperature incommensurate phase is ferroelectric and demonstrates the magnetoelectric effects [4,5].

Chemical substitutions may lead either to quantitative changes in magnetic subsystem parameters or to qualitative alteration of its type. The latter happened at partial substitution of tellurium by selenium in $Fe(Te_{1.5}Se_{0.5})O_5Cl$. The $Fe(Te_{1.5}Se_{0.5})O_5Cl$ system crystallizes in the same space group $P2_1/c$ as $FeTe_2O_5Cl$ but its structure is quite different [6]. In the crystal structure of $FeTe_2O_5X$ compounds tellurium ions partly possess quite unusual coordinations TeO_2X and TeO_3X forming the $Te_4O_{10}X_2$ groups [1]. The selenium ion is smaller and usually prefers the SeO_3E (E is a pair of electrons) pyramidal shape surrounding [6]. It could be a reason why $FeSe_2O_5X$ compounds do not exist and Te_3SeO_{10} groups form in the crystal structure of $Fe(Te_{1.5}Se_{0.5})O_5Cl$. Here, the tellurium ions are four oxygen coordinated whereas three oxygen coordinated positions are occupied by tellurium and selenium ions in a statistically equal ratio, as shown in Fig. 1 [6].

Magnetically, $Fe(Te_{1.5}Se_{0.5})O_5Cl$ features the dimers of Fe^{3+} ions formed by edge-sharing FeO_5Cl octahedra. These dimers constitute double chains running along the *c* axis in the *bc* plane. Along the *b* axis the *ac* planes are weakly coupled by van der Waals interactions. In present paper we report on studies of magnetization M and specific heat C_p, combined with Raman spectroscopy, dipole-dipole, and density functional calculations in $Fe(Te_{1.5}Se_{0.5})O_5Cl$.

II. EXPERIMENT

The single crystal of $Fe(Te_{1.5}Se_{0.5})O_5Cl$ was grown by the gas transport method, as described in Ref. [6]. The crystal structure of this compound is shown in the left panel of Fig. 1 in mixed ball-and-stick and polyhedral representation. In the right panel of Fig. 1 tentative magnetic structure of $Fe(Te_{1.5}Se_{0.5})O_5Cl$ is shown as follows from results of density functional theory (DFT) calculations and minimization of dipole-dipole interactions energy.

The temperature dependencies of magnetic susceptibility χ were taken in the temperature range 2–380 K in the field cooled (FC) regime in a magnetic field 0.1 T oriented along the principal crystallographic axes by means of vibrating sample magnetometer (VSM) option of Quantum Design Physical Properties Measurements System (PPMS) 9T. The field

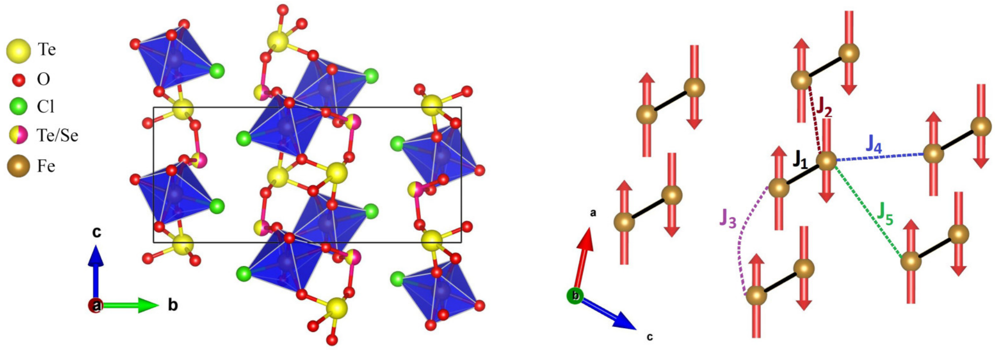

FIG. 1. Left: The crystal structure of Fe(Te$_{1.5}$Se$_{0.5}$)O$_5$Cl in mixed ball-and-stick and polyhedral representation. Iron ions are shown in the polyhedra FeO$_5$Cl; two positions of chalcogen ions are shown by unicolor and bicolor spheres. Right: The map of exchange interaction pathways in the magnetic structure of Fe(Te$_{1.5}$Se$_{0.5}$)O$_5$Cl. The spheres correspond to Fe^{3+} ions with magnetic moments represented by the arrows. All other ions are removed for clarity.

dependencies of magnetization M along a, b, and c axes were measured by Quantum Design Magnetic Properties Measurements System (MPMS) 7T at 2 K up to 7 T. The temperature dependence of specific heat C_p in the range 2–250 K has been measured using a quasiadiabatic calorimeter option of PPMS, 9T.

Raman scattering experiments were performed in quasi-backscattering geometry using a $\lambda = 532$-nm laser line of a Nd:YAG laser with a power of $P = 30\,\mu$W. The spectra were collected with a Jobin Yvon LabRam HR800 Micro Raman spectrometer and a 50×-objective. Low temperature data were obtained with the single crystal inserted in a CryoVac, He-cooled microcryostat in the temperature range 4–300 K, energy range 90-910 cm^{-1}. The sample orientation of the single crystals is random. The spectra are recorded without a polarization filter.

In order to gain microscopic understanding of the magnetic properties of Fe(Te$_{1.5}$Se$_{0.5}$)O$_5$Cl the first principles density functional theory (DFT) [7] calculations within the generalized gradient approximation [8] were carried out for the exchange-correlation functional. Calculations were performed using plane wave basis as implemented within Vienna Ab initio Simulation Package (VASP) [9] as well as muffin-tin orbital (MTO) based Nth order MTO (NMTO) [10] and linear tight-binding MTO (TB-LMTO) [11] calculations implemented in STUTTGART code. Consistency of results between two basis sets has been checked in terms of calculated density of states and band structure.

Magnetic dipole-dipole energies were calculated using self-made software based on approach similar to that outlined in Ref. [12]. Magnetic dipoles were put in the iron sites of unit cell with moments orientation corresponding to proposed magnetic structure. Then three-dimensional supercell was generated with initial unit cell positioned in the center of the structure. Magnetic dipole-dipole interaction energy of each atom of the initial cell with each atom of the generated structure was calculated. To obtain total dipole-dipole interaction energy per cell these energies were summed.

III. THERMODYNAMIC PROPERTIES

The temperature dependencies of magnetic susceptibility $\chi(T)$ of single crystal of Fe(Te$_{1.5}$Se$_{0.5}$)O$_5$Cl were measured under magnetic field B applied along a, b, and c axes as shown in Fig. 2. At elevated temperatures, all these dependencies run in parallel following the Curie-Weiss law

$$\chi = \chi_0 + \frac{C}{(T - \Theta)}, \tag{1}$$

where χ_0 is the temperature-independent term, C is the Curie constant, and Θ is the Weiss temperature. At lowering temperature, $\chi_{a,b,c}(T)$ evidences a broad hump at $T_\mathrm{M} \sim 70$ K which corresponds to the regime of short-range magnetic correlations. The fits of $\chi_{a,b,c}(T)$ dependencies can be done within spin $S = 5/2$ dimer model

$$\chi = \chi_0 + \frac{N_A g^2 \mu_B^2}{k_B T} \frac{\left[\exp\left(\frac{J_1}{k_B T}\right) + 5\exp\left(\frac{3J_1}{k_B T}\right) + 14\exp\left(\frac{6J_1}{k_B T}\right) + 30\exp\left(\frac{10J_1}{k_B T}\right) + 55\exp\left(\frac{15J_1}{k_B T}\right)\right]}{\left[1 + 3\exp\left(\frac{J_1}{k_B T}\right) + 5\exp\left(\frac{3J_1}{k_B T}\right) + 7\exp\left(\frac{6J_1}{k_B T}\right) + 9\exp\left(\frac{10J_1}{k_B T}\right) + 11\exp\left(\frac{15J_1}{k_B T}\right)\right]}, \tag{2}$$

where N_A, μ_B, and k_B are Avogadro, Bohr, and Boltzmann constants, $g = 2$ is the g factor of Fe^{3+} ions, and J_1 is the intradimer exchange interaction parameter [13]. The average value of $\chi_0 = -8.9 \times 10^{-4}$ emu/mol and the average value of $J_1 = 28$ K. The fits are shown by solid lines in Fig. 2. The inset to Fig. 2 represents the inverse magnetic susceptibility $(\chi - \chi_0)^{-1}(T)$ fitted by linear dependence which results in the negative Weiss temperature $\Theta = -118$ K.

At formation of long-range order at $T_\mathrm{N} = 22$ K, the $\chi_{a,b,c}(T)$ curves spread revealing the anisotropy of the magnetically ordered phase. While χ_a drops down and χ_c remains virtually unchanged at $T < T_\mathrm{N}$, the χ_b evidences spontaneous magnetization. The field dependencies of magnetization M in the single crystal of Fe(Te$_{1.5}$Se$_{0.5}$)O$_5$Cl are shown in Fig. 3. The $M(B)$ curve is predominantly linear at the $B//b$ axis and deviates from linearity at the $B//a$ and $B//c$ axes which means

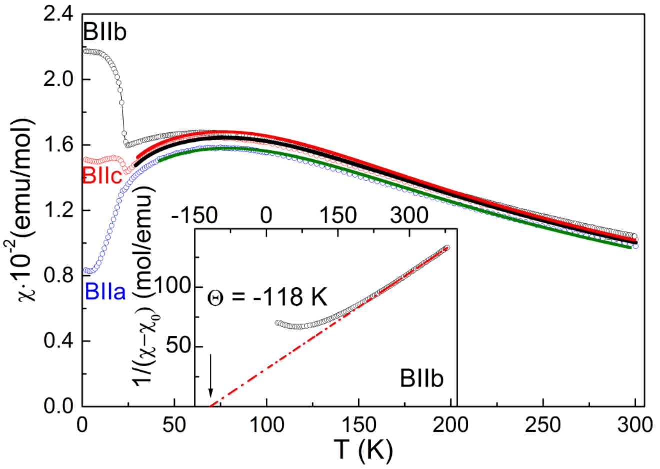

FIG. 2. The temperature dependencies of magnetic susceptibility in Fe($Te_{1.5}Se_{0.5}$)O_5Cl single crystal at $B = 0.1$ T. The fits obtained in accordance with $S = 5/2$ dimer model [13] are shown by solid lines. Inset: The temperature dependence of inverse magnetic susceptibility at elevated temperatures. The linear fit taken in the range 250–380 K is shown by dash-dotted line.

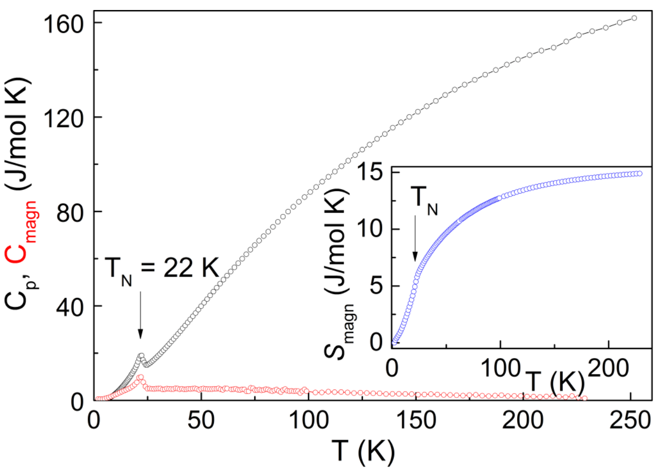

FIG. 4. The temperature dependencies of specific heat C_p and magnetic contribution to specific heat C_{magn} in Fe($Te_{1.5}Se_{0.5}$)O_5Cl. The inset represents temperature dependence of magnetic entropy S_{magn}.

that the Fe^{3+} moments lie in the *ac* plane. The $M(B)$ curve demonstrates weak hysteresis shown in the inset to Fig. 3.

The temperature dependence of specific heat C_p of Fe($Te_{1.5}Se_{0.5}$)O_5Cl is shown in Fig. 4. It shows a sharp λ-type anomaly at $T_N = 22$ K. The magnetic contribution to specific heat C_{magn} obtained in accordance with Fisher's formula [14] is shown also in Fig. 4. It was calculated using the conjecture that C_{magn} equals the derivative $\frac{\partial \chi_{\parallel} T}{\partial T}$ normalized by the coefficient K. This coefficient is a product of a number of neighboring spins z_1 ($z_1 = 1$ for dimers), intradimer exchange interaction parameter J_1, the function f equal to unity near the phase transition (and approaching $1/z_1$ at high temperatures which is also equal to 1 for dimers), anisotropy of exchange interaction α (which varies between 0 and 1 for Heisenberg and Ising models), g factor g and universal gas constant R:

$$K = \frac{3z_1 J_1 k_B f(1 - 2/3\alpha)}{N_A g^2 \mu_B^2} R. \tag{3}$$

The coefficient K was normalized so that the integral of C_{magn}/T vs T function approached the theoretical value of magnetic entropy $S_{magn} = R\ln(2S + 1) = 14.8$ J/mol K at high temperatures. This allows estimating the exchange anisotropy parameter $\alpha = 0.55$ for $J_1 = 28$ K obtained from the $\chi(T)$ data. The temperature dependence of magnetic entropy S_{magn} is shown in the inset to Fig. 4. About one-third of total magnetic entropy S_{magn} is released at $T < T_N$ meaning that the short-range magnetic correlations develop at elevated temperatures.

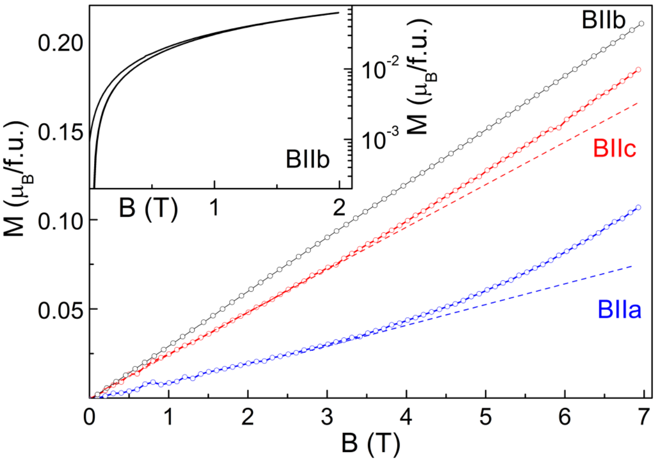

FIG. 3. The field dependencies of magnetization in Fe($Te_{1.5}Se_{0.5}$)O_5Cl at $T = 2$ K. The dotted lines are guides for the eye. Inset: The first quarter of hysteresis loop in Fe($Te_{1.5}Se_{0.5}$)O_5Cl taken at $T = 2$ K.

IV. RAMAN SCATTERING

The factor group analysis for the $P2_1/c$ space group with all atoms in 4 *e* Wyckoff positions gives a total of $10 \times (3A_g + 3B_g) = 60$ Raman-active modes [15]. The low symmetry of the atomic positions leads to partial mode overlap and various intensities. Therefore only 36 modes have been observed experimentally. Figure 5(a) presents Raman spectra of Fe($Te_{1.5}Se_{0.5}$)O_5Cl at various temperatures. The low energy part of the spectra is more intense which indicates the participation of easily polarizable Se and Te lone-pair ions. The spectra can be divided into four subgroups with respect to the frequency of the modes: [60-200; 200-520; 600-750; 750-900] cm^{-1}. The first subgroup corresponds to interlayer modes involving halide anions, the second one to Fe, Te, Se, O vibrations with Te and Se largest displacements, the third one to Fe, Te, Se, O vibrations with O largest displacement, and the fourth one is related to Fe-related modes [16]. The low energy part of the spectrum contains sharp and intense modes which become even more intense with decreasing temperatures and do not narrow much. The modes at intermediate energies demonstrate less pronounced hardening and stronger linewidth Γ decreases with decreasing temperatures. The

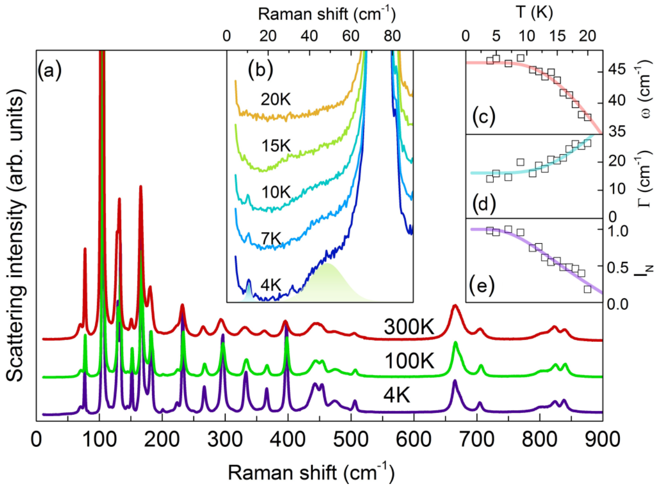

FIG. 5. (a) Raman spectra of $\mathrm{Fe(Te_{1.5}Se_{0.5})O_5Cl}$ as a function of temperature. (b) Magnetic scattering at low temperatures. The insets show the temperature dependencies of (c) frequency, (d) linewidth, and (e) intensity for the two-magnon line, with solid lines as a guide for the eye.

temperature dependence of the frequency ω is similar for all phonon groups, as shown in Fig. 6.

The increase from room temperature down to ∼70 K reflects the anharmonicity of the lattice, i.e., a decay of thermally populated optical phonons into acoustic modes. The temperature dependence of frequency and linewidth of the optical phonons are approximated by the following phenomenological fits and plotted as curves in Fig. 6:

$$\frac{\omega-\omega_0}{\omega_0} = -B - C\left(1 + \frac{D}{\exp\frac{\hbar\omega_0}{k_B T} - 1}\right), \quad \omega_0 = \omega(T \to 0), \tag{4}$$

$$\Gamma(T) = \Gamma_0\left(1 + \frac{2A}{\exp\frac{\hbar\omega_0}{k_B T} - 1}\right), \quad \Gamma_0 = \Gamma(T \to 0), \tag{5}$$

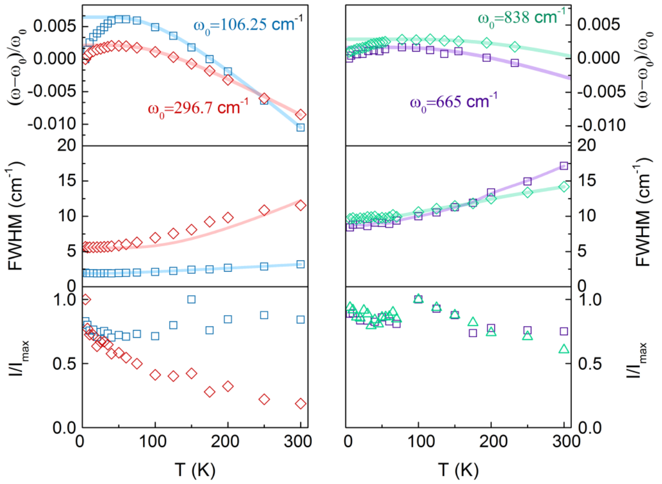

FIG. 6. Analysis of representative modes within each phonon group, including the frequency shift, linewidth, and intensity. The lines correspond to fits using a phenomenological anharmonic model, based on Eqs. (5) and (6).

TABLE I. Anharmonic law fit parameters.

Mode-dependent fit parameters	ω_0 (cm^{-1})			
	106	297	665	838
B	0.099	0.100	−0.100	0.053
C	−0.101	−0.010	0.010	−0.056
D	−0.115	−0.336	0.473	−0.760
A	0.223	1.750	7.101	6.460
Γ_0 (cm^{-1})	1.900	6.020	9.500	10.114

where A, B, C, D are the normalizing coefficients, given in Table I [17]. The observed further decrease is not related to anharmonicity and evidences a coupling of the phonons to short-range spin correlations [broad maximum at $\chi(T)$]. The intensity of a phonon has to be discussed separately, as it is related to the respective electronic polarizability. Here, it is remarkable that the group 2 phonons, related to highly polarizable, lone-pair ions Se and Te, show the strongest intensity increase with decreasing temperatures, while the mode intensities of the other frequency regimes vary with temperature in a nonmonotonic way. Furthermore, the intensity of all phonons is nonmonotonous as a function of temperature around 150 K.

At lowest temperatures additional scattering intensity appears as two maxima, as shown in Fig. 5(b). Since in this temperature range the compound is magnetically ordered, we attribute these lines to magnetic excitations. A narrow line at about 10 cm^{-1} can be assigned to one-magnon scattering and its energy is related mainly to the spin anisotropy. A broad maximum at about 47 cm^{-1} is attributed to two-magnon scattering. This is based on its higher energy and its observability up to T_N in both parallel and crossed polarizations. The position of the two-magnon scattering allows estimating the average strength of magnetic exchange coupling using the equation

$$\omega_{2\mathrm{M}} = J_1(2_{Z1}S - 1). \tag{6}$$

This approach corresponds to a counting of spin-exchange induced, broken magnetic bonds [18]. A broad maximum value leads to an average $J_1 \sim (17 \pm 0.2)$ K, which is somewhat smaller than the calculated value $J_1 = 25.5$ K of the intradimer exchange interaction parameter (see below). We attribute this difference on one hand to the rough estimation of the equation that bond breaking of a Néel state without taking spin-spin interactions into account. On the other hand there exists a large number of exchange paths with a large variation of exchange coupling strength. Therefore, the product zJ is rather ill-defined. This difference may also be discussed in the context of a two-magnon density of states that is strongly renormalized for smaller coordination numbers.

V. FIRST PRINCIPLES CALCULATIONS

The calculated non-spin-polarized and spin-polarized electronic density of states are shown in the left and right panels of Fig. 7, respectively. The states near the Fermi level are dominantly contributed by Fe d states admixed with O p and Cl p states, being primarily responsible for the electronic and

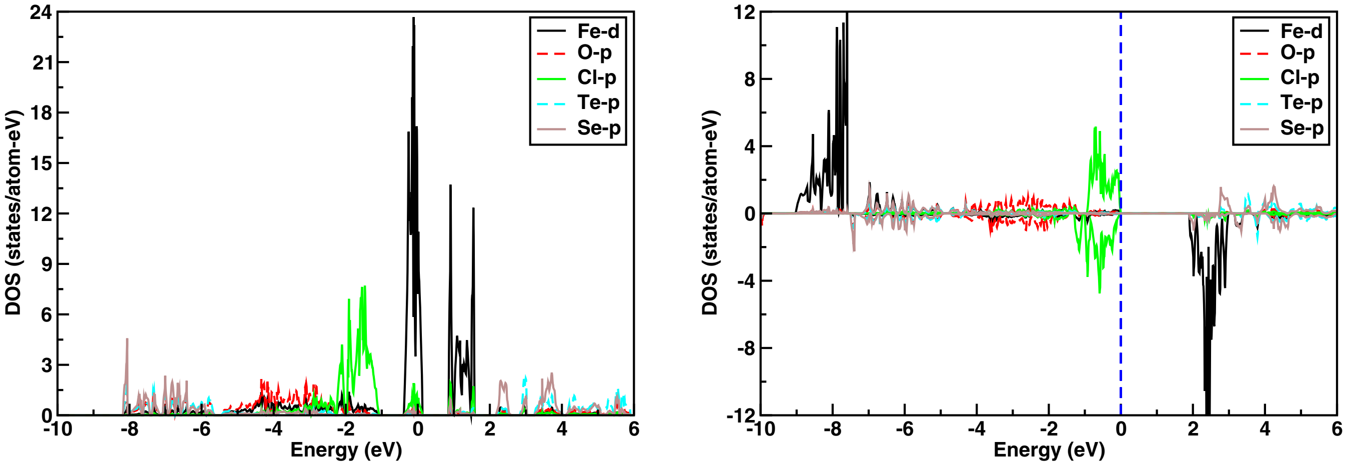

FIG. 7. Non-spin-polarized (left panel) and spin-polarized (right panel) density of states (DOS) calculated in TB-LMTO basis in Fe($Te_{1.5}Se_{0.5}$)O_5Cl. Energy axis is plotted with respect to Fermi energy.

magnetic behavior of the compound. The octahedral crystal field splitted Fe t_{2g} and e_g states are completely filled in the majority spin channel, and completely empty in the minority spin channel, suggesting the nominal Fe^{3+} or d^5 valence of iron. Both Te *p* and Se *p* states are found to be nearly empty, suggesting the nominal Te^{4+} and Se^{4+} valences, while the O *p* and Cl *p* states are found to be mostly occupied, suggesting the nominal O^{2-} and Cl^{-} valence states, respectively. The admixed O *p* and Cl *p* states contribute to the superexchange paths of the magnetic interaction between two Fe sites. The magnetic moment, calculated within the single-electron approximation of DFT, at the Fe, O, Cl, Te, and Se sites are found to be 4.39 μ_B, 0.11 μ_B, 0.10 μ_B, 0.03 μ_B, and 0.02 μ_B respectively. The relatively larger value of the magnetic moment of nominally nonmagnetic O^{2-} and Cl^{-} ions reflects the strong hybridization of O *p* and Cl *p* states with Fe *d* states.

To estimate the various Fe^{3+}–Fe^{3+} magnetic exchange interactions (t_{ij}) as well as crystal field splitting (Δ_{ij}) of different *d* orbitals of Fe present in the compound, the NMTO based downfolding technique was applied to construct Fe *d*-only Wannier functions by integrating out all the degrees of freedom associated with O, Cl, Se, and Te and keeping active only the Fe *d* degrees of freedom. This procedure captures the renormalization of Fe *d* orbitals due to hybridization with O *p*, Cl *p*, Se *p*, and Te *p*. The off-site elements of the real-space representation of the Hamiltonian in the effective Fe *d* Wannier function basis provide the effective Fe-Fe hopping interactions, t_{ij}'s, while the on-site elements provide Δ_{ij}. The information of effective Fe-Fe hopping interactions guide us in identifying the dominant Fe-Fe exchange pathways. In principle, the Fe-Fe magnetic interactions can be calculated from the knowledge of hopping interactions and crystal field splitting, together with a choice of Hubbard *U* parameters in the superexchange formula. This procedure, however, only accounts for the antiferromagnetic contributions. Thus, to obtain a more reliable estimation of magnetic exchanges, we performed total energy calculation of different spin configurations in GGA+*U* [19] scheme and extracted the dominant magnetic exchanges by mapping the DFT energies to that of the Heisenberg model. The GGA+*U* calculations were performed for a choice of $U = 6$ eV. A *U* value of 6 eV on Fe was chosen following the constraint density functional theory calculation on FeO [20]. Changing the *U* value over 1–2 eV keeps the ratio of different magnetic exchanges (*J*'s) fixed with dominant interaction J_1 showing inverse dependency with *U* value.

The paths for dominant magnetic interactions are shown in the right panel of Fig. 1. The calculated values of magnetic exchanges are listed in Table II. We find that the intradimer magnetic interaction J_1 corresponding to hopping t_1 is mediated by edge-shared Fe-O-Fe superexchange paths where the Fe-O-Fe bond angles are 106 °. The interdimer interaction J_2, corresponding to hopping t_2, is mediated by Fe-O-Te-O-Fe and Fe-O-Se-O-Fe supersuperexchange paths. The other interdimer interactions J_3, J_4, and J_5 corresponding to t_3, t_4, and t_5 are mediated by the Fe-O-Te-O-Fe supersuperexchange paths. The intradimer interaction J_1 turned out to be antiferromagnetic and the strongest among all interactions, with value $J_1 = 25.5$ K. The interdimer interactions turn to be also antiferromagnetic, an order of magnitude smaller in strength compared to J_1, i.e., $J_2 = 1.4$ K, $J_3 = 1.9$ K, $J_4 = 2.1$ K, and $J_5 = 3.5$ K. Our calculations including spin-orbit coupling

TABLE II. Paths and values of magnetic exchange interactions of Fe($Te_{1.5}Se_{0.5}$)O_5Cl.

Interaction	Path	Bond angle	Bond distance (Å)	Value (K)
Intradimer	J_1 (Fe-O-Fe)	106 °	3.29	25.5
Interdimer	J_2 (Fe-O-Te-O-Fe and Fe-O-Se-O-Fe)		4.48	1.4
	J_3 (Fe-O-Te-O-Fe)		5.18	1.9
	J_4 (Fe-O-Te-O-Fe)		5.46	2.1
	J_5 (Fe-O-Te-O-Fe)		6.52	3.5

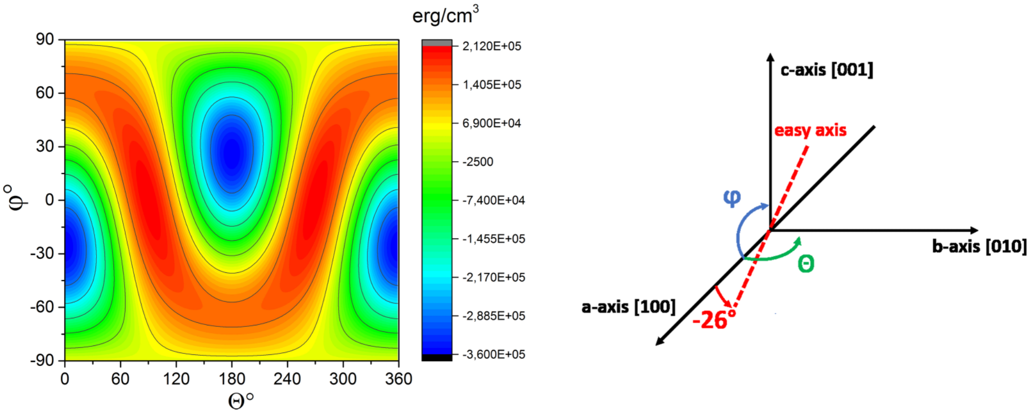

FIG. 8. Left: Energies of magnetic dipole-dipole interactions for antiferromagnetic configuration from Fig. 1, rotated around [100] direction. Right: Illustrative description of angle symbols and expected direction of antiferromagnetic easy axis.

shows a small but finite spontaneous magnetic moment, about $0.02\,\mu_B$, which cants the spins.

The estimation of Weiss temperature $\Theta = -118\,\text{K}$ from the $\chi^{-1}(T)$ curve in the range 250–380 K can be compared with the theoretical value

$$\Theta_{\text{calc}} = \sum_i \frac{z_i S(S+1) J_i}{3}, \qquad (7)$$

where z_i are the numbers of nearest neighbors for J_i interactions. Taking the values of J_i given in Table II we obtain $\Theta_{\text{calc}} = -106\,\text{K}$. This estimation however does not take into account the interlayer exchange interactions.

VI. MAGNETIC MODEL

From experimental $M(B)$ and $\chi(T)$ curves one may conclude that the magnetization easy axis lies predominantly along the [100] direction at some angle towards [001]. The spontaneous magnetic moment has its own easy axis near the [010] direction but it is relatively easy to remagnetize and flip in the opposite direction. Hysteresis loop for $B||b$ shows a small coercive field of about 300 Oe that corresponds to the energy $1.4 \times 10^3\,\text{erg/cm}^3$ that should be resulting from the competition between magnetocrystalline anisotropy and domain walls formation. There are several possible sources of magnetocrystalline anisotropy: single-ion anisotropy, shape anisotropy, classical dipole-dipole interactions, and anisotropic exchange interactions due to spin-orbit coupling. Since Fe^{3+} in the high spin $S = 5/2$ state is a highly isotropic ion, its orbital momentum is zero in ideal octahedral or tetrahedral coordination. Thus, it is unlikely to expect significant single-ion anisotropy or spin-orbit coupling contributions to anisotropy in such a case. However, in $\text{Fe(Te}_{1.5}\text{Se}_{0.5})\text{O}_5\text{Cl}$ the magnetic moment at Fe sites is expected to be $4.39\,\mu_B$ according to DFT calculations, that is less than ideal isotropic $5\mu_B$ for $S = 5/2$ state. It may be explained by nonsymmetric distorted FeO_5Cl octahedral coordination of iron ions. So, spin-orbit coupling as well as single-ion anisotropy should not be negligible.

Besides, because of the relatively large magnetic moment of the Fe^{3+} ion, a considerable contribution of magnetic dipole-dipole interactions to magnetocrystalline anisotropy should be expected. Note that in materials with high magnetic moments such as Y-type and M-type ferrites [12] and MnF_2 [21] magnetic dipole-dipole interactions exert a significant or even crucial effect on observed magnetocrystalline anisotropy [22].

We calculated total interaction energy for system of $4.39\,\mu_B$ magnetic dipoles located in Fe sites according to magnetic configuration, shown in the right panel of Fig. 1. Calculation was performed by coherent rotation of atomic moments with angular step about 1 °. Influence of atoms positioned not more than 20-unit cells away from initial cell was taken into account. We did not include a spin canting in our calculations, since its estimated value about 0.01 ° is small. Thus, produced results indicate only easy magnetization axis and do not contain information about spontaneous magnetic moment direction. The results are illustrated by Fig. 8.

According to these results, the direction of antiferromagnetic easy axis predominately in the ac plane with angle approximately 26 ° from [100] to [00$\bar{1}$] is obtained. It corresponds to energy minima in left panel of Fig. 8. Comparing the energies between the easy axis and perpendicular directions we can extract magnetic dipole-dipole contribution to anisotropy field $B_\text{A} = (2\mu_0 E_\text{A})^{-1/2} \approx 0.4\,\text{T}$ that is relatively large. Thus, magnetic dipole-dipole interactions significantly affect the magnetic system configuration choice.

VII. CONCLUSIONS

A partial substitution of Te^{4+} ions by Se^{4+} ions transforms the crystal structure of $\text{FeTe}_2\text{O}_5\text{Cl}$ drastically. The structure of $\text{Fe(Te}_{1.5}\text{Se}_{0.5})\text{O}_5\text{Cl}$ contains Fe^{3+} dimers producing short-range correlations evidenced in broad hump in temperature dependence of magnetic susceptibility at 70 K. The estimated intradimer exchange interaction is $J_1 = 28\,\text{K}$. At $T_\text{N} = 22\,\text{K}$, the specific heat demonstrates a λ-type anomaly corresponding to antiferromagnetic state formation. Both temperature and field dependencies of magnetization point to the ac easy plane of the antiferromagnetic structure. At $T < T_\text{N}$, a different mode of magnetic origin is observed in Raman spectroscopy measurements. The modeling of the magnetic structure highlights the importance of dipole-dipole interactions between Fe^{3+} ions spin moments. Spin-orbit coupling is found to be responsible for the small uncompensated moment at the Fe site associated with canting of spins. First principles calculations unveil the $J_1 - J_5$ magnetic exchange interactions; the value of intradimer exchange interaction agrees well with experimental estimations. Notably, similar iron dimers have been observed in another iron oxohalide, $FeTe_3O_7X$ (X = Cl, Br), with comparable intradimer exchange interactions [23].

ACKNOWLEDGMENTS

This work has been supported by Russian Science Foundation Grant No. 19-42-02010 and by National University of Science and Technology "MISiS" Grant No. K2-2020-008. It was supported also by Act 211 of the Government of Russian Federation, Contracts No. 02.A03.21.0004, No. 02.A03.21.0006, and No. 02.A03.21.0011. P.L. acknowledges support by Deutsche Forschungsgemeinschaft (DFG, German Research Foundation) DFG LE967/16-1 and DFG EXC-2123 QuantumFrontiers 390837967.

[1] R. Becker, M. Johnsson, R. K. Kremer, H.-H. Klauss, and P. Lemmens, J. Am. Chem. Soc. **128**, 15469 (2006).

[2] J. Chakraborty, N. Ganguli, T. Saha-Dasgupta, and I. Dasgupta, Phys. Rev. B **88**, 094409 (2013).

[3] M. Pregelj, H. O. Jeschke, H. Feldner, R. Valenti, A. Honecker, T. Saha-Dasgupta, H. Das, S. Yoshii, T. Morioka, H. Nojiri, H. Berger, A. Zorko, O. Zaharko, and D. Arcon, Phys. Rev. B **86**, 054402 (2012).

[4] M. Pregelj, A. Zorko, O. Zaharko, Z. Kutnjak, M. Jagodic, Z. Jaglicic, H. Berger, M. de Souza, C. Balz, M. Lang, and D. Arcon, Phys. Rev. B **82**, 144438 (2010).

[5] M. Pregelj, A. Zorko, O. Zaharko, P. Jeglic, Z. Kutnjak, Z. Jaglicic, S. Jazbec, H. Luetkens, A. D. Hillier, H. Berger, and D. Arcon, Phys. Rev. B **88**, 224421 (2013).

[6] A. Y. Akhrorov, E. S. Kuznetsova, S. M. Aksenov, P. S. Berdonosov, A. N. Kuznetsov, and V. A. Dolgikh, Solid State Sci. **74**, 37 (2017).

[7] W. Kohn and L. J. Sham, Phys. Rev. **140**, A1133 (1965).

[8] J. P. Perdew, K. Burke, and M. Ernzerhof, Phys. Rev. Lett. **77**, 3865 (1996).

[9] G. Kresse and J. Furthmuller, Phys. Rev. B **54**, 11169 (1996).

[10] O. K. Andersen and T. Saha-Dasgupta, Phys. Rev. B **62**, R16219(R) (2000).

[11] O. K. Andersen and O. Jepsen, Phys. Rev. Lett. **53**, 2571 (1984).

[12] A. Isalgué, X. Obradors, and J. Tejada, J. Phys. Colloq. **46**, C6-345 (1985).

[13] K. S. Murray, Coord. Chem. Rev. **12**, 1 (1974).

[14] M. E. Fisher, Philos. Mag. **7**, 1731 (1962).

[15] Bilbao Crystallographic Server; see spectral active modes, https://www.cryst.ehu.es/rep/sam.html.

[16] K. Y. Choi, I. H. Choi, P. Lemmens, J. van Tol, and H. Berger, J. Phys.: Condens. Matter **26**, 086001 (2014).

[17] P. G. Klemens, Phys. Rev. **148**, 845 (1966).

[18] K.-Y. Choi, P. Lemmens, D. Heydhausen, G. Güntherodt, C. Baumann, R. Klingeler, P. Reutler, and B. Büchner, Phys. Rev. B **77**, 064415 (2008).

[19] V. I. Anisimov, I. V. Solovyev, M. A. Korotin, M. T. Czyzyk, and G. A. Sawatzky, Phys. Rev. B **48**, 16929 (1993).

[20] V. I. Anisimov, J. Zaanen, and O. K. Andersen, Phys. Rev. B **44**, 943 (1991).

[21] D. C. Johnston, Phys. Rev. B **93**, 014421 (2016).

[22] C. Pellegrini, T. Müller, J. K. Dewhurst, S. Sharma, A. Sanna, and E. K. U. Gross, Phys. Rev. B **101**, 144401 (2020).

[23] D. Zhang, R. K. Kremer, P. Lemmens, K. Y. Choi, J. Liu, M. H. Whangbo, H. Berger, Y. Skourski, and M. Johnsson, Inorg. Chem. **50**, 12877 (2011).